

Giant excitonic magneto-optical Faraday rotation in single semimagnetic CdTe/Cd_{1-x}Mn_xTe quantum ring

Kalpana Panneerselvam¹ and Bhaskaran Muralidharan¹

¹*Department of Electrical Engineering, Indian Institute of Technology Bombay, Powai, Mumbai-400076, India**

(Dated: June 7, 2025)

Magnetic tuning of the bound exciton states and corresponding giant Zeeman splitting (GZS) between σ^+ and σ^- excitonic transitions in CdTe/Cd_{1-x}Mn_xTe quantum ring has been investigated in the Faraday configuration for various concentrations of Mn²⁺ ions at different temperatures, using the variational technique in the effective mass approximation. The sp-d exchange interaction between the localized magnetic impurity ions and the delocalized charge carriers has been accounted via mean-field theory with the inclusion of modified Brillouin function. The enhancement of the GZS, and in turn, the effective Landé g-factor with the application of an external magnetic field is strikingly manifested in type-I – type-II transition in the band structure, which has been well explained by computing the overlap integral between the electron and hole, and the in-plane exciton radius. This highlights the extraordinary magneto-optical properties, including the giant Faraday rotation and associated Verdet constant, which have been calculated using a single oscillator model. The oscillator strength and exciton lifetime have been estimated and are found to be larger than in the bulk diluted magnetic semiconductors and quantum wells, reflecting stronger confinement inside the quantum ring. The results show that the DMS-based quantum ring exhibits more extensive Zeeman splitting and Faraday rotation which are a few orders of magnitude larger than in the existing quantum systems and magneto-optical materials.

I. Introduction

Diluted magnetic semiconductors (DMS) are of special interest for the past few decades because of its unique combination of semiconducting and magnetic properties. The sp-d exchange interaction between the localized magnetic moments of the dopant magnetic ions and the spins of the charge carriers (electrons/holes) in DMS [1–6] significantly alters the energy spectra of the carriers, which greatly enhances the spin dependent effects. Moreover, these effects can be widely tuned by the external magnetic field, temperature and the concentration of magnetic ions to induce fascinating magneto-optical (MO) and magneto-electrical properties. Among all the exciting signatures of such exchange interaction, the striking consequences are the giant Zeeman splitting (GZS) [7–9] and the giant Faraday rotation (GFR) [10, 11]. The Zeeman splitting between the band states with different spin components generates the spin – polarization of the conducting carriers which is exploited as spin aligners in spintronic devices [12, 13], an anomalous magnetoresistance at low temperature [14], and vastly amplifies the conversion of spin current into an electrical current [15]. Hence, the DMS have been an active area of research as an alternative to the ferromagnetic metal contacts for the efficient spin-injection into non-magnetic semiconductors, spin detection, and the realization of the spin-polarized transport in semiconductor structures, which have substantial industrial applications in the field of magnetoelectronics, spintronics, and solid-state quantum

computing [16–22]. The concept of the FR (a solid rotation of the plane of polarization of light travels in a magnetized medium along the applied magnetic field) manifests itself in various MO devices such as optical isolators, Faraday rotators, and optical circulators for high-speed optical communication systems [11, 23–25], for which DMS act as potential MO materials.

The carrier localization and its transport properties have been examined using DMS materials in various nanostructured systems like quantum wells, wires, and dots [26–29]. Considerable attention paid to quantum ring (QR)-based infrared photodetectors and lasers [30, 31] in recent times due to its doubly-connected topological nature has engendered an interest in us to study how the radial and axial confinement of the individual carriers and the exciton in semimagnetic QR impact the sp-d exchange interaction in the Faraday configuration (magnetic field is applied along the direction of observation (z) and parallel to the light wave vector). The strong sp-d coupling makes magnetic ions mediate the influence of the magnetic field on the band gap engineering by enhancing the Zeeman splitting of the energy levels, which is strikingly manifested in type-I – type-II transition in the band offset [32–35]. Hence, DMS extends its potential applications to optoelectronics due to the possible tuning of the band states, which in turn tune the emission wavelength widely over Near- to Far-IR, creating a giant optical response.

This article aims to delineate the magnetic tuning of exciton energy states due to the GZS between σ^+ and σ^- spin components, in turn the effective Landé g-factor for various mole fractions of (x) magnetic dopants at different temperature baths in CdTe/Cd_{1-x}Mn_xTe QR since CdMnTe has well served as a potential MO material for the past few decades

* bm@ee.iitb.ac.in

towards optoelectronic applications. Various MO parameters have been evaluated such as oscillator strength, radiative lifetime, and radiative decay rate. The occurrence of type-I - type-II transition in a single semimagnetic QR has been well explained in the present communication by computing the overlap integral between the electron and hole, and also estimating the in-plane exciton radius. Though QRs are more flexible for experimental developments [30, 36–39] due to the advances in fabrication procedures, and DMS addresses the fundamental challenges in the spintronic devices in its unique way, the possible integration of DMS into QR structures has not been yet developed to unveil the hidden mystery. Few theoretical studies have been proposed on single and concentric double QRs doped with transition metal ions focusing on the magnetic and thermal properties [40–42] but not on the MO properties of excitons which is of novel interest in the present work.

We later show a theoretical evaluation of the Verdet constant of a remarkable MO phenomenon, the GFR, using single oscillator model. The source for the larger values of the Verdet constant in DMS has been traced down to the GZS of the energy band states near the band gap resonance. Although most research has focused on achieving a larger Verdet constant with various MO materials, especially $\text{Cd}_{1-x}\text{Mn}_x\text{Te}$, these studies have been restricted only to bulk DMS [10, 43–46] and epitaxial heterostructures in the form of wells [47–51] and dots [11, 25, 52]. Therefore, investigating the impact of sp-d exchange interaction on the GFR in DMS heterostructures with various topologies, like QR, would generate unprecedented interest in developing high-quality epitaxial structures for various technological applications.

In the following, sec. II A discusses the theoretical formalism using the variational technique in the effective mass approximation to solve for single-particle (electron and hole) energy states in a QR doped with 10% Mn^{2+} ions at liquid helium temperature. The mean-field theory with the modified Brillouin function to account for sp-d exchange interaction is also explained in detail. Section II B discusses the solution for the excitonic case and delineates the occurrence of the GZS in nanostructures. Section III A presents the results of the binding energy of single-particle energy states under the influence of the external magnetic field for various dimensions of the QR. The results of temperature-dependent variation of interband transition energy, binding energy of σ^\pm magneto-exciton, and various MO properties, including GZS, and GFR in QR doped with various concentrations of Mn^{2+} ions ($x = 0.5\%$, 1% , 5% , 10% , and 20% of Mn^{2+} ions) are presented and discussed in sec. III B–III F. Section IV elucidates the significance of the experimental validation in QR based on DMS by comparing the present results with those already reported for the bulk and QWs.

II. Theoretical Model

A. Single-particle energy states

This section discusses the energy states of a single-particle (electron/hole) confined in a $\text{CdTe}/\text{Cd}_{0.9}\text{Mn}_{0.1}\text{Te}$ QR. The schematic diagram of the single quantum ring (SQR) is displayed in Fig. 1(a). The Schrodinger equation and corresponding Hamiltonian for the single-particle energy states subjected to magnetic flux in DMS QR is written in a dimensionless form, considering the effective Rydberg (R^*) as a unit of energy and effective Bohr radius (a_B^*) as a unit of length, and is given by,

$$\hat{H}_{e,h}\Psi_{e,h} = E_{e,h}\Psi_{e,h}; \hat{H}_{e,h} = \hat{H}_{0e,h} + \hat{H}_{sp-d} \quad (1)$$

$$\hat{H}_{0e,h} = -\nabla^2 - \frac{2}{r_{e,h}} + V_B(\rho_{e,h}, z_{e,h}) + \frac{\gamma^2 \rho_{e,h}^2}{4} + \frac{\gamma L_{ze,h}}{2} \quad (2)$$

where, e, and h represent the electron and hole, respectively, and $r_{e,h} = \sqrt{\rho_{e,h}^2 + z_{e,h}^2}$ gives the electron (hole) location from the donor (acceptor) impurity. The strength of the magnetic field is parametrized by $\gamma = \frac{\hbar\omega_c}{2R^*}$, ω_c is the cyclotron frequency, and $\gamma = 1$ corresponds to $\approx 30\text{Tesla}$ (885 Tesla) for the donor (acceptor) impurity. $L_{ze,h}$ is the z component of the orbital angular momentum of electron and hole along the 'z' direction. The sp-d exchange interaction between the electron (hole) and the localized Mn^{2+} magnetic dopants is denoted by \hat{H}_{sp-d} , which causes the Zeeman splitting of both the conduction and valence band edges in the semimagnetic ($\text{Cd}_{1-x}\text{Mn}_x\text{Te}$) barrier, and is written as [4, 53],

$$\hat{H}_{sp-d} = - \sum_i J(\mathbf{r}_{e,h} - \mathbf{R}_i) \hat{\mathbf{S}}_i \cdot \hat{\mathbf{s}}_{e,h} \quad (3)$$

'J' is the coupling constant for the exchange interaction between the electron (hole) of spin $\hat{\mathbf{s}}_e$ ($\hat{\mathbf{s}}_h$) located at \mathbf{r}_e (\mathbf{r}_h) and the spin $\hat{\mathbf{S}}_i$ of the Mn^{2+} ions located at sites \mathbf{R}_i . $V_B(\rho_{e,h}, z_{e,h})$ in Eq. (2) is the confining potential of the SQR and is modeled by an abrupt square potential:

$$V_B(\rho_{e,h}, z_{e,h}) = \begin{cases} 0 & R_1 < \rho_{e,h} \leq R_2, \\ -d/2 < z_{e,h} \leq +d/2 & \\ V_{0e,h} & \text{otherwise} \end{cases} \quad (4)$$

$V_{0e} = 70\% \Delta E_g^B$, and $V_{0h} = 30\% \Delta E_g^B$ represent the potential band offset formed in the conduction and valence band, respectively. Tuning of the potential barrier height, V_{0e} and V_{0h} with the applied field, B, is possible due to the Zeeman splitting of the band edges, which is well established through the formulation used

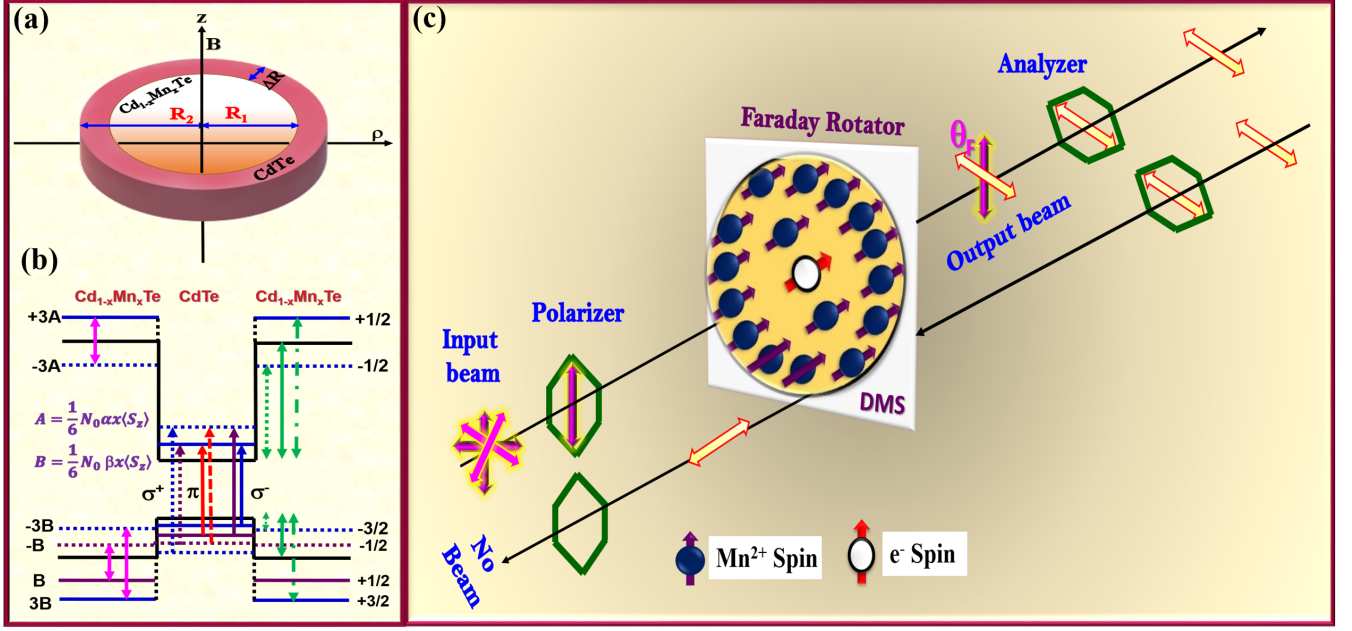


FIGURE 1. Schematics: (a) Profile of the CdTe/Cd_{1-x}Mn_xTe SQR. (b) Giant Zeeman splitting of excitonic energy levels in CdTe/Cd_{1-x}Mn_xTe and corresponding optical transitions (σ^+ , σ^- , π). (c) The concept of Faraday rotation in DMS SQR.

for bulk DMS and can be written as [32, 54],

$$\begin{aligned} V_m^e(B) &= \pm \alpha_{exc} s_e x_{eff} N_0 \langle S_z^{Mn}(B) \rangle \text{ and,} \\ V_m^{hh}(B) &= \pm \frac{1}{3} \beta_{exc} s_{hh} x_{eff} N_0 \langle S_z^{Mn}(B) \rangle \end{aligned} \quad (5)$$

Here, x_{eff} is the effective concentration of Mn²⁺ ions, and α_{exc} (β_{exc}) is the exchange constant for the conduction band (valence band), which is parametrized for Cd_{1-x}Mn_xTe as $\alpha_{exc}N_0 = 220\text{meV}$ ($\beta_{exc}N_0 = -880\text{meV}$) with the atomic concentration of Cd to be $N_0 = 1.4701 \times 10^{22}\text{cm}^{-3}$. $\langle S_z^{Mn}(B) \rangle$ is the thermal average of the spin projection of Mn²⁺ ions with spin $S_{Mn} = 5/2$ along the direction of B, and is given by the modified Brillouin function, B_S , as follows [4, 53]:

$$\langle S_z^{Mn}(B) \rangle = \left\langle \Psi_{e(h)}^w | S_0(x_{in}) B_S(y_1) | \Psi_{e(h)}^w \right\rangle + \left\langle \Psi_{e(h)}^b | S_0(x_{out}) B_S(y_2) | \Psi_{e(h)}^b \right\rangle \quad (6)$$

$$\begin{aligned} B_S(y_j) &= \frac{2S+1}{2S} \coth \frac{2S+1}{2S} y_j - \frac{1}{2S} \coth \frac{y_j}{2S} \\ y_j &= \frac{g_{Mn} \mu_B S_{Mn} B}{k_B (T + T_{AF})} \end{aligned} \quad (7)$$

$g_{Mn} = 2.01$ is the g-factor of the Mn²⁺ ion, μ_B is the Bohr Magneton, k_B is the Boltzmann constant and T is the lattice temperature. For the DMS of arbitrary 'x', the antiferromagnetic interactions between the nearest neighbouring Mn²⁺ ions are included in the calculation through the phenomenological fitting parameters, S_0 and T_{AF} , whose numerical values are obtained from the

available experimental results [1]. In order to investigate the variation of potential barrier with the magnetic field, K. Navaneethakrishnan et al [55] have suggested a formula that satisfactorily fits the experimental data available for the Mn²⁺ compositions $x = 0.07, 0.24,$ and 0.3 with a maximum error of 5%. Hence, the same formula is adopted here, and the fitting equation and corresponding discussion are given in Appendix A. The variational ansatz of the ground state donor (acceptor) impurity in a SQR includes the envelope Bessel function $\phi(\rho_{e,h}, \varphi_{e,h})$ along the radial confinement and the envelope function $f(z_{e,h})$ along the z-direction and is defined as,

$$\Psi_{e,h} = N_{1s,e,h} \phi(\rho_{e,h}, \varphi_{e,h}) f(z_{e,h}) \exp^{-\lambda r_{e,h}} \quad (8)$$

$$\phi(\rho_{e,h}, \varphi_{e,h}) = \begin{cases} C_{1,e,h} J_0(\beta_{e,h}, \rho_{e,h}), & \rho_{e,h} < R_1 \\ C_{2,e,h} J_0(\alpha_{e,h}, \rho_{e,h}) + \\ C_{3,e,h} Y_0(\alpha_{e,h}, \rho_{e,h}), & R_1 \leq \rho_{e,h} \leq R_2 \\ C_{4,e,h} K_0(\beta_{e,h}, \rho_{e,h}), & \rho_{e,h} > R_2 \end{cases} \quad (9)$$

$$f(z_{e,h}) = \begin{cases} B_{e,h} \exp[k_{e,h} z_{e,h}], & z_{e,h} < -d/2 \\ \cos(\kappa_{e,h} z_{e,h}), & -d/2 < z_{e,h} < +d/2 \\ B_{e,h} \exp[-k_{e,h} z_{e,h}], & z_{e,h} > d/2 \end{cases} \quad (10)$$

$$\text{where, } \beta_{e,h} = \frac{m_b^*(V_{0e,h} - E_{\rho_{e,h}})}{\hbar^2} \quad ; \quad \alpha_{e,h} = \frac{m_w^* E_{\rho_{e,h}}}{\hbar^2}$$

$$k_{e,h} = \frac{m_b^*(V_{0e,h} - E_{z_{e,h}})}{\hbar^2} \quad ; \quad \kappa_{e,h} = \frac{m_w^* E_{z_{e,h}}}{\hbar^2}$$

$E_{\rho_{e,h}}, E_{z_{e,h}}$ are the subband energy levels formed due to

the radial and axial confinement of the QR. The binding energy of the donor (acceptor) impurity is obtained by the equation,

$$E_{Be,h} = E_{\rho_e,h} + E_{z_e,h} + \gamma - \langle \mathbf{H}_{e,h} \rangle_{min} \quad (11)$$

B. Magnetic tuning of exciton energy levels

Within the effective mass approximation, the Schrodinger equation and corresponding Hamiltonian of the ground state electron-hole pair confined in a SQR is written as,

$$\hat{H}_{ex} \Psi_{ex} = E_{ex} \Psi_{ex} \quad (12)$$

$$\begin{aligned} \hat{H}_{ex} = & -\frac{1}{\rho_e^2} \frac{\partial^2}{\partial \varphi^2} - \frac{1}{\rho_h^2} \frac{\partial^2}{\partial \varphi^2} - \frac{\mu(T)}{m_e^*(T)} (\nabla \rho_e^2 + \nabla z_e^2) \\ & - \frac{\mu(T)}{m_h^*(T)} (\nabla \rho_h^2 + \nabla z_h^2) + V(\rho_e, z_e) + V(\rho_h, z_h) \quad (13) \\ & - \frac{e^2}{\epsilon(T) |\vec{r}_e - \vec{r}_h|} + i\gamma \frac{m_h^* - m_e^*}{m_h^* + m_e^*} \frac{\partial}{\partial \varphi} + \frac{\gamma^2 \rho^2}{4} \end{aligned}$$

Since the electron and hole move freely along the annular part of the ring, their motion no longer depends on φ_e and φ_h separately, but on the relative angular displacement $\varphi = \varphi_e - \varphi_h$, and it should be treated with the reduced effective mass ' μ ' of the exciton. Moreover, the material parameters, effective mass, and spatial dielectric constant are considered as temperature-dependent. The most appropriate trial wavefunction of a ground state exciton is written in a non-separable form due to correlated electron-hole pair as,

$$\Psi_{ex}(r_e, r_h) = N_{1s} \phi(\rho_e, \rho_h) f(z_e, z_h) \Omega(\rho_e, \rho_h, z_e, z_h, \varphi) \quad (14)$$

where, $\Omega(\rho_e, \rho_h, z_e, z_h, \varphi) = e^{-\lambda r_{eh}}$ describes the correlation between the electron and hole which depends mainly on the distance, $r_{eh} = \sqrt{|\rho_e - \rho_h|^2 + |z_e - z_h|^2}$ between the two, whereas, $|\rho_e - \rho_h|^2$ denotes the projection of the distance between the electron and hole on the plane of the QR and is given by, $|\rho_e - \rho_h|^2 = (\rho_e^2 + \rho_h^2 - 2\rho_e\rho_h \cos(\varphi))^{1/2}$. Invoking the variational technique, the binding energy ($E_{B_{ex}}$) and the interband transition energy ($E_{T_{ex}}$) of the exciton is computed using the form,

$$\begin{aligned} E_{B_{ex}} &= E_{\rho_e} + E_{\rho_h} + E_{z_e} + E_{z_h} + \gamma - \langle \mathbf{H}_{ex} \rangle_{min} \quad (15) \\ E_{T_{ex}} &= E_g(T) + \langle \mathbf{H}_{ex} \rangle_{min} \end{aligned}$$

In the Faraday geometry, the magnetic moments of the ensemble of Mn^{2+} ions with spin angular momentum $S_{Mn} = 5/2$ are subjected to the sp-d exchange interaction with the conduction band electrons of spin $s = 1/2$ and

the heavy hole valence band with angular momentum $J = 3/2$. This causes the heavy hole exciton splits into two components with angular momentum $+1$ and -1 which is composed of $s_z = -1/2$, $J_z = +3/2$ and $s_z = 1/2$, $J_z = -3/2$, respectively. The GZS between the excitonic energy levels exhibited in the nanostructures is as similar as in bulk DMS, but with a difference in the potential barrier height experienced by the two different spin states. The schematic diagrams which explain the Zeeman splitting of the energy levels in DMS nanostructures and its resultant GFR are depicted in Fig. 1(b) and Fig. 1(c). The applied magnetic field increases and decreases the potential barrier for the spin up and spin down states, respectively, and thereby the corresponding confinement of both the electron and heavy hole with $s_z = +1/2$, $J_z = +3/2$, and $s_z = -1/2$, $J_z = -3/2$ becomes stronger and weaker, respectively, inside the QR. Therefore, by magnetically tuning the potential barrier, the energy levels of the exciton inside the QR could also be tuned, manifesting itself in two different excitonic transitions, namely σ^+ and σ^- . σ^+ corresponds to the transition between $J_z = -3/2$ (heavy hole) and $s_z = -1/2$ (electron) states, and σ^- transition involves $J_z = +3/2$ and $s_z = +1/2$ states. The splitting of the energy level corresponding to two transitions is expressed by [1],

$$E_{\pm} = \pm \frac{1}{2} x_{eff} N_0 (\beta_{exc} - \alpha_{exc}) \langle S_z^{Mn}(B) \rangle \quad (16)$$

The Zeeman splitting energy between the two excitonic transitions and its relation to the magnetization, M , is given by [1, 43],

$$\Delta E_z^{sp-d} = E_+ - E_- = \frac{\beta_{exc} - \alpha_{exc}}{g_{Mn} \mu_B} M \quad (17)$$

The effective Landé g- factor, g_{eff} , corresponding to the exciton Zeeman splitting is calculated by,

$$\Delta E_z^{sp-d} = g_{eff} \mu_B B \quad (18)$$

III. Results and Discussion

A. Binding energy of the donor and acceptor impurities

The numerical calculations have been done for various outer radii (R_2) and heights (d) of the QR, keeping the inner radius of the ring constant to $R_1 = 50\text{\AA}$. The results for the single-particle energy states in the absence of magnetic field have already been reported in our previous work [40]. In the present communication, a series of calculations have been performed for various strengths of the magnetic field by varying the ring width from 30 to 350 \AA , keeping 'd' constant to $d = 10, 20, 40, 150,$ and 200\AA , and the results are compared with the results

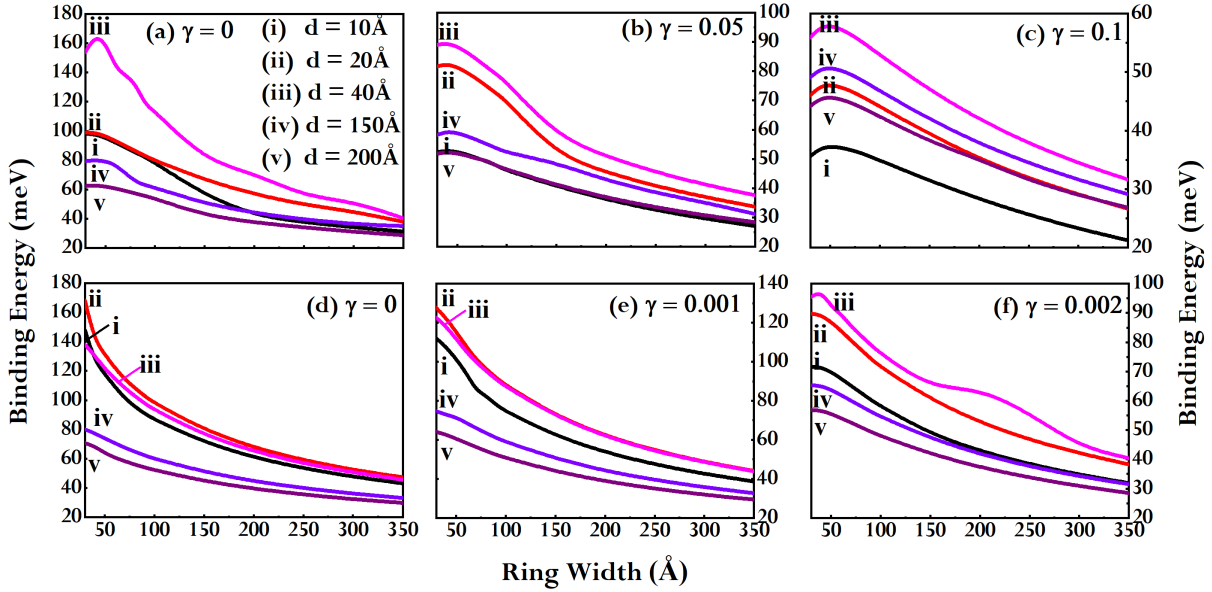


FIGURE 2. Impurity binding energy *vs* ring width at different strengths of the magnetic field for various heights of the ring. *Upper Panel:* Donor Impurity (a) $\gamma = 0$, (b) $\gamma = 0.05$, and (c) $\gamma = 0.1$. *Lower Panel:* Acceptor Impurity (a) $\gamma = 0$, (b) $\gamma = 0.001$, and (c) $\gamma = 0.002$.

reported in Ref [40]. Figure 2(a)-2(c) shows the binding energy of the donor impurity as a function of ring width ($R_2 - R_1 = R$) for different values of ‘d’ by placing the impurity at the centre of the radial ($\rho_i = (R_1 + R_2)/2$) and the axial direction ($z_i = 0$) of the QR.

For a given height of the ring, the binding energy shows a non-monotonic behaviour irrespective of the applied magnetic field, when the ring width increases from narrow to a bulk limit which is a signature of any low dimensional system. E_B increases until it reaches a maximum at a particular value of ‘R’, which falls in the quasi 1-D region, and thereafter it decreases monotonically due to the delocalization of the wavefunction. However, the decrease of binding energy below the quasi 1-D region is attributed to the penetration of the carrier wavefunction through CdMnTe barrier. In the absence of magnetic field, this non-monotonicity as a function of ‘R’ is visible only for $d = 40\text{\AA}$, and the maximum is seen at $R = 30\text{\AA}$, which is a favourable ring width at which the carrier is strongly bound to the impurity and is shifted to higher R values when B starts to increase. The impurity states are susceptible to the external magnetic field, as could be seen from a rapid fall of binding energy as B increases from $\gamma = 0.05$ (1.5Tesla) to $\gamma = 0.1$ (3Tesla). This is because, the magnetic field tremendously reduces the potential barrier height as a result of the interaction between the Mn^{2+} impurity ions residing in the barrier and the localized carriers in the well region, which in turn reduces the confinement, and the binding energy peaks at a ring width shifted to higher values.

The above discussion is also applicable for the heavy hole bound to an acceptor impurity (Fig. 2(d)-2(f)) confined inside such QR, except for the following: The acceptor binding energy is larger than the donor’s binding energy irrespective of the magnetic field. This is mainly due to the larger effective mass of the hole ($m_h^* = 0.67$) than the electron’s effective mass ($m_e^* = 0.090$). Moreover, no conspicuous turnover is seen in the binding energy as a function of R_2 for the system with ($\gamma = 0.001$ (0.8Tesla), $\gamma = 0.002$ (1.5Tesla)), and without ($\gamma = 0$) the application of magnetic field. Most importantly, in the absence of B, the promising height of the ring, which gives maximum confinement for the hole is $d \approx 20\text{\AA}$ rather than $d \approx 40\text{\AA}$ as in the case of donor.

The same can be noticed by comparing Fig. ??(a) with Fig. ??(b) in Appendix B, which depicts the variation of binding energy as a function of ‘d’ for different outer radii ‘ R_2 ’ and magnetic field. It is seen from both these figures that the binding energy increases as ‘d’ decreases and shows a maximum at a specific value of ‘d’ and then drops slowly for further reduction of the height of the ring, which is again a tell-tale hallmark of any low dimensional system. As the outer radius increases, the peak value of the binding energy is suppressed, and there is a shift in the peak when the system is subjected to the external magnetic field.

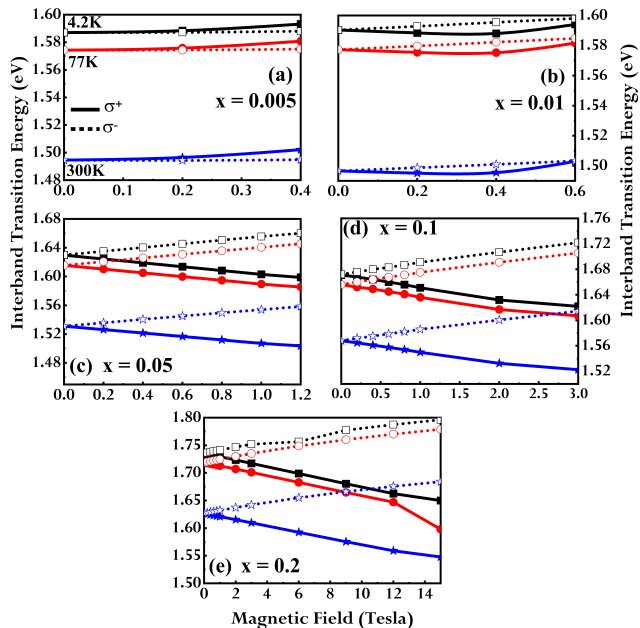


FIGURE 3. Interband transition energy as a function of magnetic field for σ^+ and σ^- exciton at different temperatures for various dopant concentrations. (a) $x = 0.005$, (b) $x = 0.01$, (c) $x = 0.05$, (d) $x = 0.1$, and (e) $x = 0.2$.

B. Magnetic-field induced excitonic interband transition energy

Magnetic field dependence of the PL transition energy (E_T) for both σ^+ and σ^- polarization for various concentrations of Mn^{2+} ions at different temperatures is computed for ring dimensions $R = 80\text{\AA}$, $d = 20\text{\AA}$, which is approximately equals to the effective Bohr radius of the exciton, and the results are displayed in Fig. 3. The transition energy increases with the increasing concentration of Mn^{2+} ion because the bandgap (E_g) is directly proportional to the latter and decreases with increasing temperature since E_g has a negative temperature coefficient. The calculation using the above theoretical model shows that at $B = 0$, the PL is unpolarized, i.e., the energies of σ^\pm magneto-exciton are degenerate. However, the applied magnetic field breaks the degeneracy and causes the PL to split into left (σ^-) and right (σ^+) circularly polarized. This is indicated by a monotonic shift of E_T towards low and high energies about zero field energy in Fig. 3, and the PL gets resolved into two branches of exciton doublet corresponding to σ^+ and σ^- polarization, respectively. The reason for this is attributed to the fact that the applied magnetic field influences the potential barrier height of the two different spin components in a unique way owing to the sp-d exchange interaction, as discussed in sec. II B.

The variation of E_T with B for the QR doped with low Mn^{2+} concentration ($x \leq 0.01$) is different from the QR doped with high concentration. Instead of showing

a rapid fall with the magnetic field as seen for higher concentration, the σ^+ transition energy mimics the σ^- transition, as shown in Fig. 3(a) and 3(b), indicating a change of the PL emission from right circular to left circular polarization. A vivid picture of this unusual behaviour for low 'x' has been well explained in a DMS QD by Kai Chang et al [29], which is ascribed to the tuning of the effective g-factor to zero with the increasing field when the order of Zeeman splitting due to sp-d exchange interaction is comparable to the order of intrinsic Zeeman splitting. The sign of the former is opposite to the latter. The presence of crossing between σ^+ and σ^- transition energy in Ref [29] is missing here for $x = 0.01$ because the data has been plotted for the extended range of magnetic fields, including the type-II region in Ref [29], whereas it is limited to the type-I region in the present work. Typically, the order of intrinsic Zeeman splitting is much smaller than the energy level splitting induced by the sp-d exchange interaction; hence, the former is neglected in the present calculation.

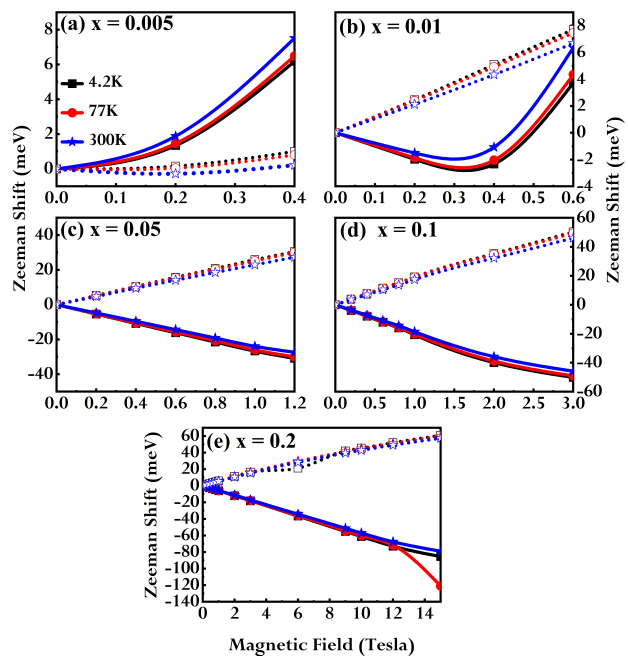


FIGURE 4. Zeeman shift related to zero field magneto-exciton energy *vs* magnetic field for various dopant concentrations at different temperatures. (a) $x = 0.005$, (b) $x = 0.01$, (c) $x = 0.05$, (d) $x = 0.1$, and (e) $x = 0.2$.

C. Zeeman shift and Zeeman splitting of the exciton energy levels

Figure 4 plots the magnetic field dependence of the exciton transition energy as Zeeman shifts ($E_{\text{ex}}(B) - E_{\text{ex}}(B = 0)$) relative to the zero-field exciton

energy for both the transitions, which is also described by Eq. (16). It is noted from figure that the shift increases with increasing magnetic field for both the transition, but it shows a positive and negative increment for σ^- and σ^+ which corresponds to the blue and redshift in the interband transition energy (Fig. 3), respectively. Interestingly, one could observe the symmetric Zeeman splitting about the zero-field energy for the QR doped with 5% and 10% of Mn^{2+} ions, but for all other dopant concentrations (0.5%, 1%, and 20%), the splitting seems to be asymmetric.

On the quantitative footing, the Zeeman splitting energy, $\Delta E_z^{\text{sp-d}}$, plotted in Fig. 5(a) for $x = 0.05$ is described as the energy difference between the two excitonic transitions under B and is determined from the data plotted in Fig. 4 as given in Eq. (17). The numerical data for $x = 0.005, 0.1,$ and 0.2 are depicted in Fig. ??(a)-??(c) in Appendix C. Two opposing parameters, the magnetic field, and temperature, interplay with each other to determine the Zeeman splitting. The magnetic field suppresses the Mn^{2+} spin fluctuations by aligning the randomly oriented Mn^{2+} spins along the field direction, indicating a state of magnetic ordering, thereby increasing $\langle S_z \rangle$ and causing the GZS. Contradicting this, the spin fluctuations are large enough to keep the state with a maximum entropy at elevated temperatures, and eventually, the Zeeman splitting is abated by the thermal energy. It is interesting

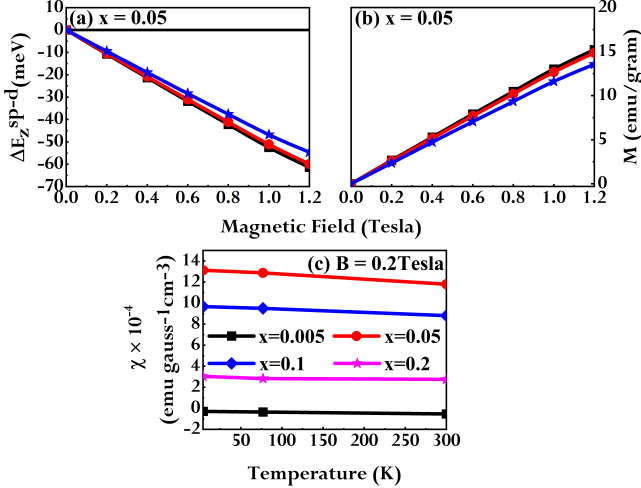


FIGURE 5. (a) Zeeman splitting ($\Delta E_z^{\text{sp-d}}$) of the 1s exciton at various temperatures for $x = 0.05$. (b) Temperature dependent magnetization (M) calculated using modified Brillouin function for $x = 0.05$. (c) Magnetic susceptibility (χ) data for various dopant concentrations as a function of temperature.

to note from Fig. 5(a) and (??) that $\Delta E_z^{\text{sp-d}}$ increases with the dopant concentration up to $x = 0.05$, and thereafter it starts decreasing. This is because the Zeeman splitting is proportional to the effective dopant concentration ' x_{eff} ' as given in Eq. (16), and the latter

increases with 'x' and shows a maximum at a particular concentration. Henceforth, it starts to move downhill because of the antiferromagnetic interactions between the nearest neighbouring magnetic ions, which cancels the spins of the corresponding pairs and reduces the effective contribution to the thermal average of the spin polarization of Mn^{2+} ions, $\langle S_z \rangle$. In the framework of the theoretical model described in sec. IIB, the effect of temperature on the absolute value of effective Landé g-factor has been calculated, and the results are tabulated in Table-I for various 'x'. The enhanced g-factor in the applied magnetic field directly evidences the strength of the Zeeman splitting, and the reduction in g-factor for increased temperature is also anticipated because of the depolarization of Mn^{2+} spins.

TABLE I. Effective Landé g-factor at $T = 4.2\text{K}$ and 300K .

Effective Landé g-factor (g_{eff}) at $B = 0.2\text{Tesla}$		
x	T = 4.2K	T = 300K
0.005	102.375	186.451
0.01	-383.885	-313.412
0.05	-928.099	-820.949
0.1	-681.671	-601.917
0.2	-202.032	-195.048

Figure 5(b) shows the magnetization (M) vs magnetic field curves at different temperatures for $x = 0.05$. Magnetization increases with the magnetic field since it enhances $\langle S_z \rangle$, showing a linear dependence on magnetic field, which is an expected paramagnetic behaviour and does not saturate even at higher magnetic fields, $B > 10\text{T}$. Similarly, it decreases when temperature augments, restricting all the magnetic moments from aligning along the field direction by intensifying the spin fluctuations so that the magnetic ordering is hampered. As already discussed, when QR is populated with more magnetic ions, the spin-spin interaction becomes more robust, which results in a quenching of magnetization for high 'x' because of the lower value of $\langle S_z \rangle$ (Fig. ??(d)-??(f) in Appendix C). To corroborate these results, the temperature dependent magnetic susceptibility, χ , data for various concentrations keeping the magnetic field constant to $B = 0.2\text{Tesla}$ is illustrated in Fig. 5(c).

D. Binding energy of σ^\pm magneto-exciton

The variation of binding energy is plotted in Fig. 6(a) for $x = 0.05$. The trend of the binding energy for both σ^- and σ^+ polarization concerning the magnetic

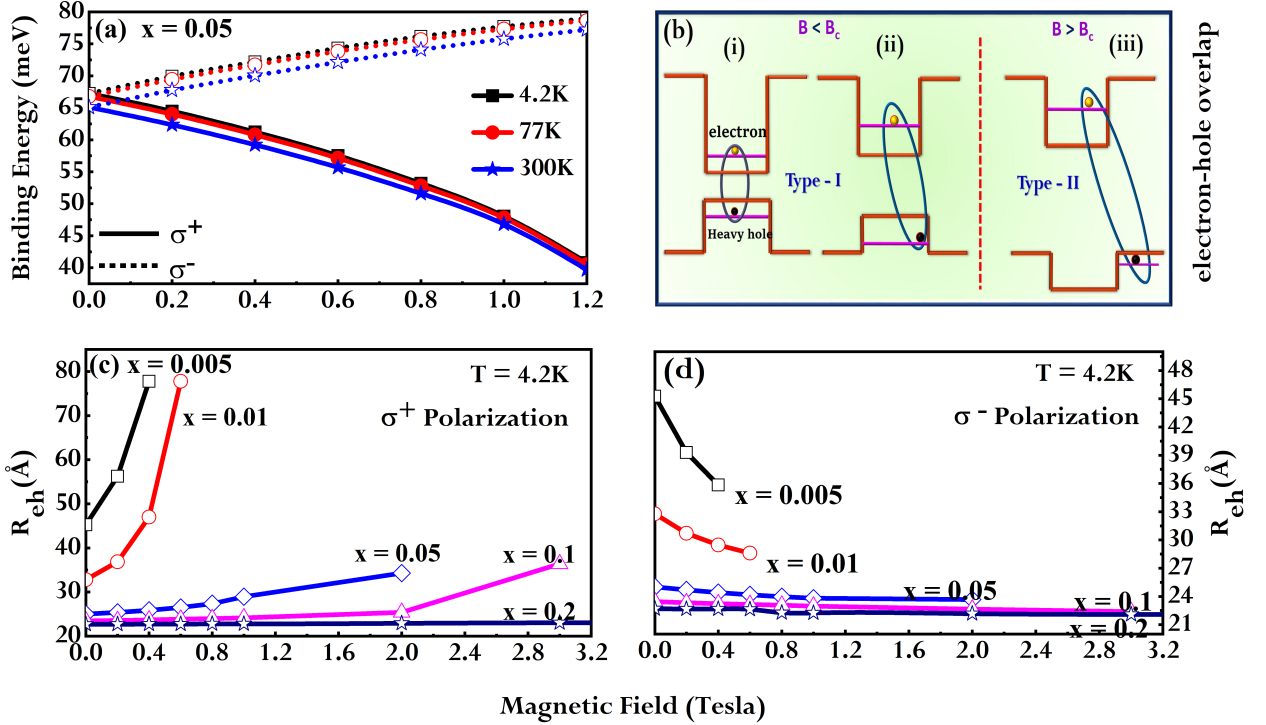


FIGURE 6. (a) Binding energy of σ^\pm magneto-exciton *vs* magnetic field for $x = 0.05$ at different temperatures. In-plane electron-hole distance corresponding to (b) σ^+ and (c) σ^- exciton *vs* magnetic field for various dopant concentrations at $T = 4.2K$. (d) Schematic explaining the overlap integral between the electron and hole under various strengths of magnetic field. (i) $B = 0$, (ii) $0 < B < B_c$, and (iii) $B > B_c$.

field is as same as the trend followed by the interband transition energy, and this behaviour persists at different temperatures and concentrations. Nevertheless, for σ^+ polarization, there is a rapid decrease of binding energy with the magnetic field as compared to the steady increase for σ^- polarization. This can be better understood from the schematic in Fig. 6(b), which explains how the applied magnetic field modifies the electron-hole overlap inside a SQR.

At $B = 0$, the location of both the electron and hole is in the same CdTe layer (Fig. 6(b-i)). Zeeman splitting of the energy levels in the valence band is highly sensitive to the applied field, which is not the case with the conduction band. This is because the band offset formed in the conduction band is generally larger than the valence band offset since 80% of the bandgap difference falls in the former. Moreover, the absolute value of the exchange constant, which represents the strength of the exchange interaction, is larger for the heavy hole ($|\beta_{exc}N_0 = 880\text{meV}|$) than for the electron ($|\alpha_{exc}N_0 = 220\text{meV}|$). Therefore the electron with $s_z = -1/2$ in the conduction band would forever be confined in the non-magnetic CdTe layer itself irrespective of the strength of the applied field

as its potential band offset is sufficiently larger than the order of magnetic splitting (Fig. 6(b-ii)). However, the potential barrier for the heavy hole with $J_z = -3/2$ is tremendously reduced with the magnetic field, and it encounters a flat band situation at critical field value, beyond which the system undergoes a type-I - type-II transition (Fig. 6(b-iii)). As a result, the electron remains in the CdTe layer, but the hole moves towards the heterostructure interface and finally to the CdMnTe layer. Hence, the exciton will no longer be spatially direct; rather, it becomes spatially indirect, which reduces the overlap between the electron and hole, whereby spin-down exciton states have reduced binding energy.

To justify this discussion, the in-plane exciton radius, R_{eh} , the average distance between the electron and hole in the plane of the QR, has been calculated and is plotted in Fig. 6(c) and 6(d). As anticipated, the monotonic increase and decrease of R_{eh} could be seen for σ^+ and σ^- polarization, respectively, for all x . Moreover, the 3D plot of the probability distribution of spin-down electrons and holes ($|\Psi|^2$) along ρ and z -directions of the QR, and the density plot of the single-particle distribution depicted in Fig. 7 helps to understand the effect of magnetic field on

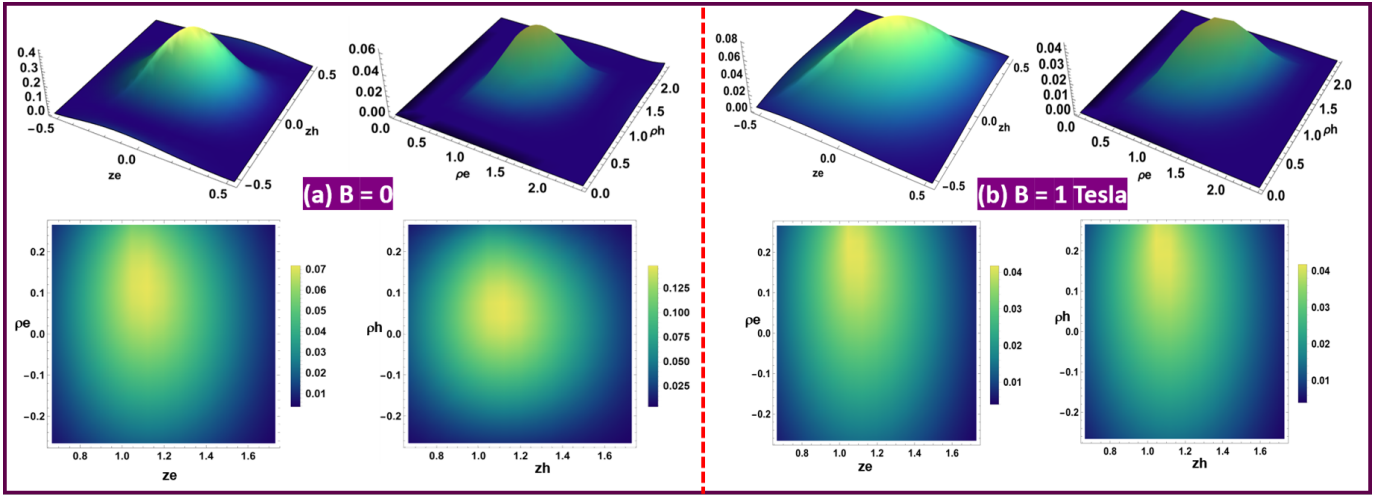


FIGURE 7. *Left panel*: 3D-plot for the probability distribution of electrons and holes along axial, and radial direction. *Right panel*: Density plot of the probability distribution of single-particle states along both radial and axial direction. The data has been plotted for (a) $B = 0$, and (b) $B = 1$ Tesla.

the carrier confinement inside the QR. Obviously, $|\Psi|^2$ is larger for zero magnetic field as one can compare the order of magnitude between $B = 0$ and $B = 1$ Tesla.

E. Oscillator strength, radiative linewidth and radiative lifetime of magneto-exciton

To gain further insight into the σ^+ and σ^- transition and related radiative properties, the investigation of oscillator strength (OS), radiative decay rate (RDR), and radiative lifetime (RLT) have been performed, and the results are delineated. The expression for the exciton oscillator strength follows [48, 56, 57],

$$f_{\pm} = \frac{E_P}{2E_{T\pm}} \left| \int_{-\infty}^{+\infty} I d\rho_e dz_e \right|^2 |\Omega(0)|^2 \quad (19)$$

where, $E_P = 2.1\text{eV}$ for CdTe, represents the Kane energy. The OS mainly depends on the overlap integral 'I' between the electron and hole envelope wavefunctions: $I = \left| \int_{-\infty}^{+\infty} N_{1s} \phi_e(\rho_e) \phi_h(\rho_e) f_e(z_e) f_h(z_e) d\rho_e dz_e \right|^2$, and $\Omega(0)$ denotes the probability of finding the electron and hole at the same position. The oscillator strength per unit area is proportional to the effective Bohr radius as, $F_{\pm} = \frac{1}{a_B^2} f_{\pm}$. Exciton radiative lifetime, ' τ ' (radiative decay rate, ' $\Gamma = 1/\tau$ ') can be related to OS according to [58, 59],

$$\tau = \frac{2\pi\epsilon_0 m_0 c^3 \hbar^2}{n e^2 E_{T\pm} f_{\pm}} \quad (20)$$

Here, the fundamental physical constants have their usual meaning and 'n' represents the refractive index of the material CdTe.

The evolution of the oscillator strength as a function of magnetic field solely depends on the spatial overlap

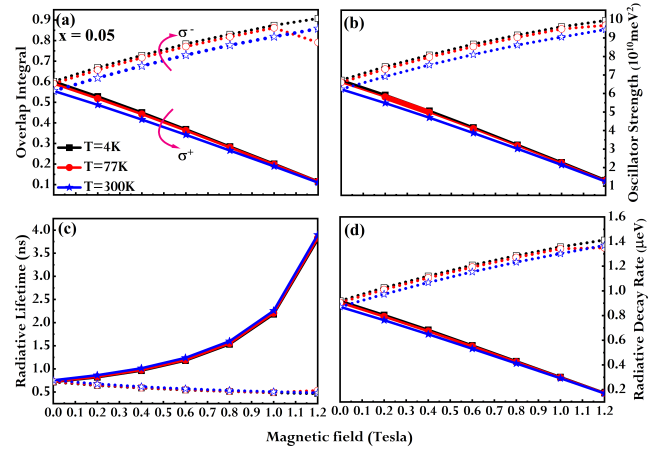


FIGURE 8. Temperature dependent variation of (a) overlap integral, (b) oscillator strength, (c) radiative lifetime, and (d) radiative decay rate with magnetic field for σ^+ and σ^- transitions for $x = 0.05$.

between the electron and hole wave functions, which has been depicted for $x = 0.05$ in Fig. 8. The numerical data pertaining to all other concentrations are depicted in Fig. ?? and ?? in Appendix D. The applied magnetic field increases the overlap between the electron and hole ground states for σ^- polarization, indicating larger OS due to the increase of potential barrier height. As expected for the σ^+ polarization, the OS sensitively depends on B, which diminishes the excitonic effect by spatially separating the electron and hole as explained in sec. III D and thereby weakens the corresponding optical transition. The overlap integral is suppressed by the thermal energy $k_B T$, whereby the oscillator strength is also abated. The overlap integral increases as the dopant concentration increases due to the increased potential

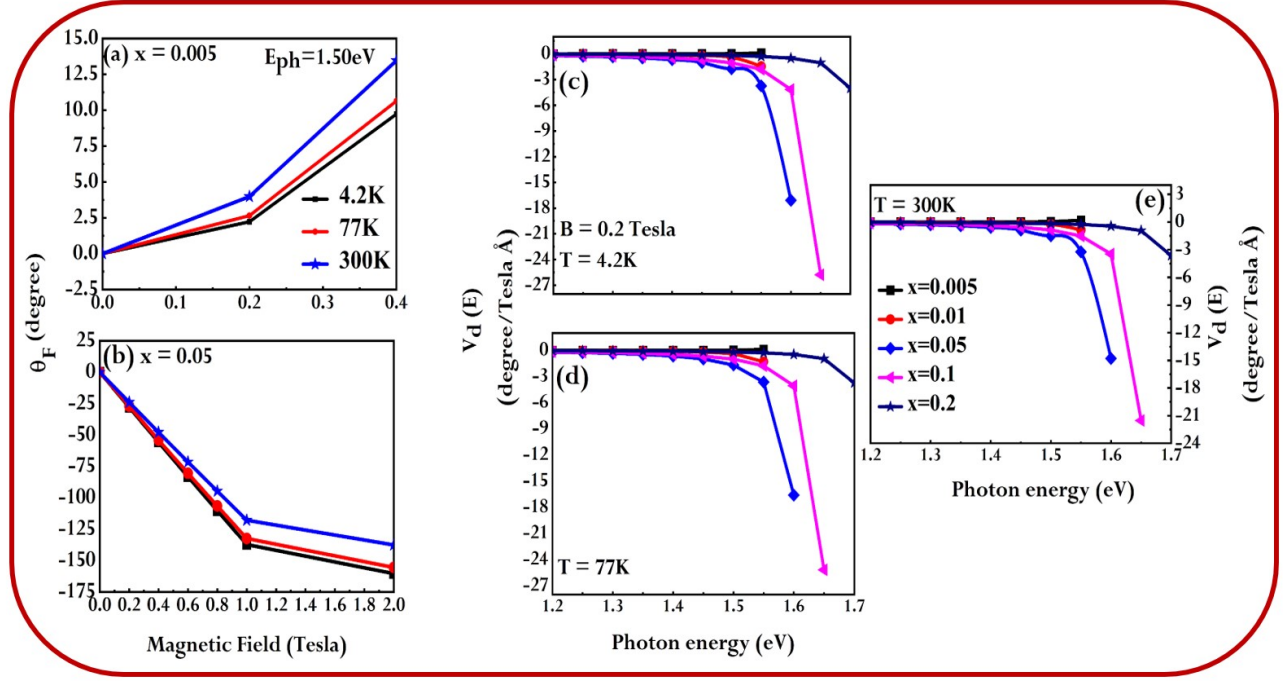


FIGURE 9. Faraday rotation angle (Θ_F) as a function of magnetic field for (a) $x = 0.005$, and (b) $x = 0.05$ at different temperatures for a fixed photon energy of $E=1.50\text{eV}$. Verdet constant as a function of photon energy for various dopant concentrations at (c) $T = 4.2\text{K}$, (d) $T = 77\text{K}$, and (e) $T = 300\text{K}$ for a fixed strength of magnetic field, $B = 0.2\text{Tesla}$.

barrier height (Fig. ??).

Figure 8(c) and 8(d) shows the radiative lifetime and radiative decay rate as a function of magnetic field for 5% of Mn^{2+} concentration. The RLT of exciton increases with increasing B for σ^+ polarization, which is accompanied by a decrease in RDR. The exciton lifetime is found to decrease from 5.04ns to 0.38ns when the concentration of Mn^{2+} ion increases from $x = 0.005$ to $x = 0.2$ at low temperature and at $B = 0$, where radiative recombination dominates (Fig. ??). The RDR, which characterizes the decay of photon emitted by the exciton, shows its maximum only for $B = 0$, which elucidates the probability of finding an electron and hole at the same position ($r_e = r_h$) is more prominent in the absence of magnetic field.

F. GFR in semimagnetic SQR

The Faraday rotation (Fig. 1(c), also known as an optical analogue of the Hall Effect, results from a difference in refractive indices of the left and right circularly polarized light after traveling through a magnetized medium with a length ‘ l ’. If there is a difference in absorption of two circularly polarized light, then the polarization vector will change its helicity from linear to elliptical. However, in the present work, only the changes in refractive indices are considered in the numerical calculations and the latter is ignored. The

phase difference in velocity between the two circularly polarized components is expressed through the FR angle as [43],

$$\Theta_F = \frac{\Delta\phi}{2} = \frac{El}{2\hbar c} (n_- - n_+) \quad (21)$$

Here, n_- and n_+ denote the refractive indices of the left and right circularly polarized light, and E is the incident photon’s energy. As aforementioned, the FR in DMS alloys is a giant one due to the large Zeeman splitting of the energy levels as a result of sp-d exchange interaction, which has been computed using the single oscillator model as preferred in the work of Bartholomew et al., After performing a series of calculations, Θ_F achieves the final form as [43],

$$\Theta_F = \frac{\sqrt{F_0}l}{2\hbar c} \left(\frac{\beta_{exc} - \alpha_{exc}}{g_{Mn} \mu_B} \right) M \frac{1}{E_0} \frac{y^2}{(1 - y^2)^{3/2}}; y = \frac{E}{E_0} \quad (22)$$

Here, F_0 is a constant that involves the oscillator strength, and E_0 is the ground state interband transition energy at the fundamental energy gap at zero magnetic field. The angle is directly proportional to the GZS through the term $\Delta E = \frac{\beta_{exc} - \alpha_{exc}}{g_{Mn} \mu_B} M$. The Verdet constant is written as the Faraday rotation per unit

magnetic field per unit length, which is defined as [43],

$$V_d(E) = \frac{\Theta_F}{Bl} = \frac{\sqrt{F_0}}{2\hbar c} \left(\frac{\beta_{exc} - \alpha_{exc}}{g_{Mn} \mu_B} \right) \frac{\partial M}{\partial H} \frac{1}{E_0} \frac{y^2}{(1-y^2)^{3/2}} \quad (23)$$

Figure 9(a) and 9(b) depicts Θ_F for the DMS QR in the dilute regime ($x=0.005$) and doped with arbitrary 'x' ($x = 0.05$) at a fixed photon energy of 1.5eV. It is noted from figure that the rotation angle increases with the increasing magnetic field since the applied field enhances the Zeeman splitting and decreases with the temperature since the magnetization is suppressed at elevated temperatures. The variation of the Verdet constant with the incident photon energies at different temperatures for a fixed magnetic field of $B = 0.2$ Tesla is plotted in Fig. 9(c)-9(e). The Verdet constant shows a sharp increase whenever the band gap resonance occurs (when the energy of the incident photon approaches the absorption edge of the material), and the photon energy, at which the Verdet constant shows a rapid enhancement, shifted to higher energies for the heavily doped QR because the absorption edge increases as the concentration of Mn^{2+} ions increases. Though the single oscillator model yields gratifying results, in which the behaviour of E_0 at Γ point has been crudely modelled as constant at all temperatures, the success of using this in QR could not be verified due to a lack of reliable experimental data.

IV. Concluding Remarks

Probing the single-particle and exciton energy states in an applied magnetic field has been studied in semimagnetic QR, and the theoretical investigation of tuning related MO properties has been attempted. It is found that the doubly-connected topological structures like QR provide robust confinement for the carriers compared to single-connected topological QDs [60]. The difference in the behaviour of magneto-exciton energies between the QR doped with low and high Mn^{2+} ion concentrations has been explained in detail at various temperatures. The results show pronounced excitonic Zeeman splitting for low 'x and T' than high 'x and T', where the possibilities for the manganese ions to form antiferromagnetic pairs in the latter case are maximized. Among all the concentrations discussed here, $x = 0.05$ exhibits larger Zeeman splitting with the absolute value of effective g-factor, $g_{eff} = 928$ (Table I, and the corresponding Verdet constant is as large as -15 degree/Tesla Å, and the latter is $10^4 - 10^6$ orders of magnitude larger than in bulk $Cd_{1-x}Mn_xTe$ [10, 43, 46], thin films [61–63], and is 10^2 orders larger than in QWs [48, 50], superlattices [49, 64] as reported in the previous studies. This elucidates the importance of DMS-based QR in MO devices operating at a wavelength shorter than $1\mu m$ than already existing MO materials, such

as Yttrium Iron Garnet (YIG) and Terbium Aluminum Garnet (TAG), organic molecules, conjugated polymers [25, 43, 65].

Moreover, the low-temperature exciton lifetime is 715ps, whereas it is ≈ 100 ps in QWs doped with 25% Mn^{2+} ion concentration [66]. The study of exciton lifetime in semimagnetic quantum systems is impressive since it affects the optical properties and the magnetization dynamics of the concerned systems to a greater extent. The exciton lifetime in DMS determines the formation of bound magnetic polaron (BMP) [67, 68] or exciton magnetic polaron (EMP) [69], which causes spontaneous ferromagnetic ordering even in the absence of an external magnetic field due to the strong sp-d exchange interaction. Since the recombination limits the exciton lifetime, it interrupts the EMP formation before the polaron reaches its stable state. If the exciton does not decay during the process of EMP formation, then the EMP would reach its equilibrium state, which is accompanied by a decrease of exciton energy and provides an additional localization for the carriers. The unique capability of manipulating the MO properties at the nanoscale in external magnetic fields and effective magnetic switching of the spins makes DMS-based QR a judicious choice among promising candidates for applications in future spintronic and optoelectronic devices. The reliability of the results obtained using the single oscillator model could not be verified due to the missing experimental data, but it is believed to be improved using the multi oscillator model as adopted in [44]. Since the low path length and the modest magnetic field yields a high Verdet constant, theoretical demonstration of generating larger FR and higher Verdet constant in DMS QRs would incite interest in preparing high-quality QR heterostructures based on DMS.

With the unrivaled ability to modulate the magnetic excitonic transitions and thereby the optical activity of the materials at the nanoscale for a broader energy spectrum with various mole fractions of Mn^{2+} ions, the diluted magnetic semiconductors have potential applications in spin-photonics and spin-electronic devices.

Appendix

A. Fitting equation for magnetic field variation of potential barrier height

The fitting equation to represent the changes in the potential barrier height as a function of magnetic field is given by [4, 53, 55],

$$\Delta E_g^B = \Delta E_g^0 \frac{\eta_{e,h} e^{\zeta_{e,h} \gamma} - 1}{\eta_{e,h} - 1} \quad (\text{A1})$$

ΔE_g^B and ΔE_g^0 denotes the band gap difference between the well CdTe layer and the barrier $\text{Cd}_{1-x}\text{Mn}_x\text{Te}$ layer in the presence and absence of applied magnetic field, respectively. The composition and temperature dependence of the latter is written as: $\Delta E_g^0(x, T) = \Delta E_g(x) + T C(x)$; $C(x)$ is known as temperature coefficient and $\Delta E_g(x) = E_g(\text{Cd}_{1-x}\text{Mn}_x\text{Te}) - E_g(\text{CdTe}) = 1.587x$. Temperature dependent band gap of the CdTe material is given by, $E_g(\text{CdTe}) = E_g(0) - \frac{\delta T^2}{T + \xi}$; $E_g(0) = 1.606 \text{ eV}$, $\delta = 4.37 \times 10^{-4} \text{ eV/K}$, $\xi = 126.8 \text{ K}$. $\eta_{e,h} = e^{\zeta_{e,h} \gamma_0}$ is chosen with a fitting parameter $\zeta_e(\zeta_h) = 0.5(-0.5)$, and γ_0 is a critical magnetic field at which the barrier completely vanishes. The critical magnetic field γ_0 in Tesla for different magnetic dopant compositions is given for donor (acceptor) impurity as $\gamma_0 = A e^{nx}$ with $A = 0.734$ and $n = 19.082$ ($A = -0.57$ and $n = 16.706$).

B. Binding energy comparison between donor and acceptor impurities

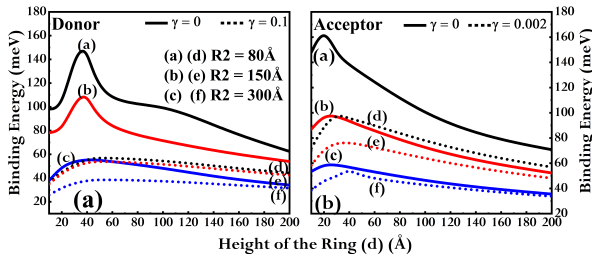


FIGURE B.1. Binding energy *vs* 'd' at different strengths of the magnetic field for various ring widths. (a) donor impurity, and (b) acceptor impurity.

C. Zeeman splitting and magnetization in dilute and high 'x' regimes

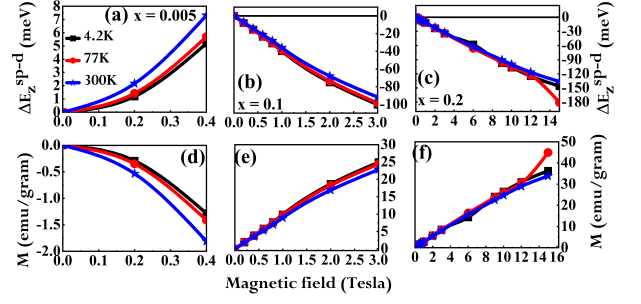


FIGURE C.1. Zeeman splitting of the excitonic energy levels ($\Delta E_z^{\text{sp-d}}$), and temperature dependent magnetization (M) in (a), (d) dilute and (b), (c), (e), (f) high x regimes.

D. Magneto-optical data for dilute and high 'x' regimes

Temperature dependent variation of the overlap integral, OS, and RLT, RDR as a function of magnetic field for 0.5%, 10%, and 20% dopant concentrations are plotted in Fig. ?? and ??, respectively.

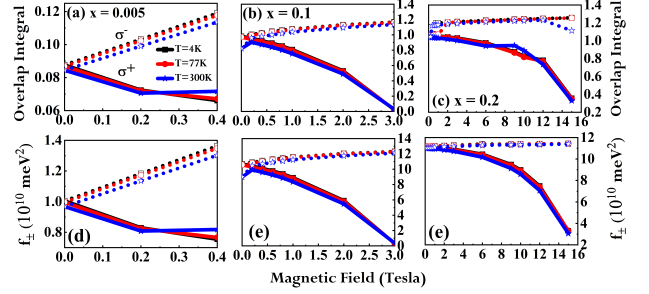


FIGURE D.1. Overlap integral (I) and oscillator strength (f_{\pm}) as a function of magnetic field for σ^+ and σ^- transition at different temperatures in (a), (d) dilute and (b), (c), (e), (f) high x regimes.

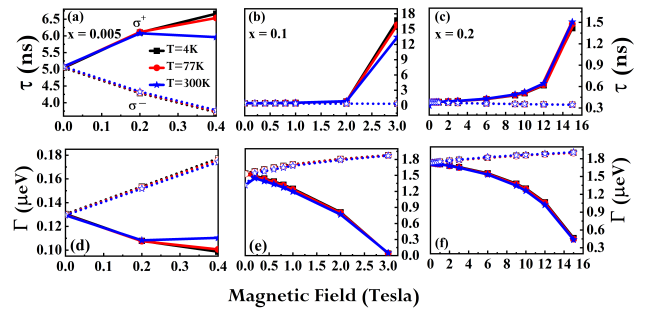


FIGURE D.2. Radiative lifetime (τ) and radiative decay rate (Γ) as a function of magnetic field for σ^+ and σ^- transition at different temperatures in (a), (d) dilute and (b), (c), (e), (f) high x regimes.

-
- [1] J. Gaj, R. Planel, and G. Fishman, *Solid State Communications* **88**, 927 (1993).
- [2] V. Y. Ivanov, M. Godlewski, D. Yakovlev, M. Kneip, M. Bayer, S. Ryabchenko, and A. Waag, *Physical Review B* **78**, 085322 (2008).
- [3] W. Rice, W. Liu, V. Pinchetti, D. Yakovlev, V. Klimov, and S. Crooker, *Nano letters* **17**, 3068 (2017).
- [4] P. S. Kalpana, P. Nithiananthi, and K. Jayakumar, *Superlattices and Microstructures* **102**, 246 (2017).
- [5] B. Anitha and P. Nithiananthi, in *AIP Conference Proceedings*, Vol. 2265 (AIP Publishing LLC, 2020) p. 030067.
- [6] N. Kozyrev, R. Akhmadullin, B. Namozov, Y. G. Kusrayev, G. Karczewski, and T. Wojtowicz, *Physical Review B* **104**, 045307 (2021).
- [7] B. Kuhn-Heinrich, W. Ossau, E. Bangert, A. Waag, and G. Landwehr, *Solid state communications* **91**, 413 (1994).
- [8] R. Fainblat, C. J. Barrows, E. Hopmann, S. Siebeneicher, V. A. Vlaskin, D. R. Gamelin, and G. Bacher, *Nano letters* **16**, 6371 (2016).
- [9] C. J. Barrows, R. Fainblat, and D. R. Gamelin, *Journal of Materials Chemistry C* **5**, 5232 (2017).
- [10] J. Gaj, R. Gatazka, and M. Nawrocki, *Solid State Communications* **88**, 923 (1993).
- [11] R. P. Panmand, S. P. Tekale, K. D. Daware, S. W. Gosavi, A. Jha, and B. B. Kale, *Journal of Alloys and Compounds* **817**, 152696 (2020).
- [12] G. Schmidt and L. W. Molenkamp, *Journal of Applied Physics* **89**, 7443 (2001).
- [13] D. Ferrand, A. Wasiela, S. Tatarenko, J. Cibert, G. Richter, P. Grabs, G. Schmidt, L. Molenkamp, and T. Dietl, *Solid state communications* **119**, 237 (2001).
- [14] T. Fukumura, Z. Jin, A. Ohtomo, H. Koinuma, and M. Kawasaki, *Applied physics letters* **75**, 3366 (1999).
- [15] S. Ganichev, S. Tarasenko, V. Bel'kov, P. Olbrich, W. Eder, D. Yakovlev, V. Kolkovskiy, W. Zaleszczyk, G. Karczewski, T. Wojtowicz, *et al.*, *Physical review letters* **102**, 156602 (2009).
- [16] T. Hirase, H. Koyama, M. Nagata, J. Ishihara, and K. Miyajima, *Journal of Physics: Condensed Matter* **31**, 425403 (2019).
- [17] I. Yahia, G. Sakr, T. Wojtowicz, and G. Karczewski, *Semiconductor science and technology* **25**, 095001 (2010).
- [18] T. Kanaki, H. Yamasaki, T. Koyama, D. Chiba, S. Ohya, and M. Tanaka, *Scientific reports* **8**, 1 (2018).
- [19] H. Terada, S. Ohya, and M. Tanaka, *Applied Physics Express* **15**, 033001 (2022).
- [20] Y. Ohno, D. Young, B. a. Beschoten, F. Matsukura, H. Ohno, and D. Awschalom, *Nature* **402**, 790 (1999).
- [21] F. Moro, L. Turyanska, J. Granwehr, and A. Patane, *Physical Review B* **90**, 205428 (2014).
- [22] J. Kobak, T. Smoleński, M. Goryca, M. Papaj, K. Gietka, A. Bogucki, M. Koperski, J.-G. Rousset, J. Suffczyński, E. Janik, *et al.*, *Nature communications* **5**, 1 (2014).
- [23] A. E. Turner, R. L. Gunshor, and S. Datta, *Applied Optics* **22**, 3152 (1983).
- [24] S. Ju, Y. Lee, Y.-T. Ryu, S. G. Kang, J. Kim, P. R. Watekar, B. H. Kim, Y. Lee, Y. H. An, C. J. Kim, *et al.*, *physica status solidi (a)* **216**, 1800549 (2019).
- [25] K. J. Carothers, R. A. Norwood, and J. Pyun, *Chemistry of Materials* **34**, 2531 (2022).
- [26] Y. Oka, K. Kayanuma, S. Shirotori, A. Murayama, I. Souma, and Z. Chen, *Journal of luminescence* **100**, 175 (2002).
- [27] K. Chang and F. Peeters, *Physical Review B* **68**, 205320 (2003).
- [28] D. Awschalom and N. Samarth, *Journal of magnetism and magnetic materials* **200**, 130 (1999).
- [29] K. Chang, J. Xia, and F. Peeters, *Applied physics letters* **82**, 2661 (2003).
- [30] B. le Feber, F. Prins, E. De Leo, F. T. Rabouw, and D. J. Norris, *Nano letters* **18**, 1028 (2018).
- [31] R. Samadzadeh, M. Zavvari, and R. Hosseini, *Optical and Quantum Electronics* **47**, 3555 (2015).
- [32] P. Klar, J. Watling, D. Wolverson, J. Davies, D. Ashenford, and B. Lunn, *Semiconductor science and technology* **12**, 1240 (1997).
- [33] E. Deleporte, J. Berroir, G. Bastard, C. Delalande, J. Hong, and L. Chang, *Superlattices and microstructures* **8**, 171 (1990).
- [34] C. Delalande, *Superlattices and microstructures* **12**, 387 (1992).
- [35] S. Kuroda, K. Kojima, K. Takita, K. Uchida, and N. Miura, *Journal of crystal growth* **159**, 967 (1996).
- [36] N. Kleemans, I. Bominaar-Silkens, V. Fomin, V. Gladilin, D. Granados, A. G. Taboada, J. García, P. Offermans, U. Zeitler, P. Christianen, *et al.*, *Physical review letters* **99**, 146808 (2007).
- [37] M. Bayer, M. Korkusinski, P. Hawrylak, T. Gutbrod, M. Michel, and A. Forchel, *Physical review letters* **90**, 186801 (2003).
- [38] F. Ding, N. Akopian, B. Li, U. Perinetti, A. Govorov, F. Peeters, C. B. Bufon, C. Deneke, Y. Chen, A. Rastelli, *et al.*, *Physical Review B* **82**, 075309 (2010).
- [39] B. Hackens, F. Martins, T. Ouisse, H. Sellier, S. Bollaert, X. Wallart, A. Cappy, J. Chevrier, V. Bayot, and S. Huant, *Nature Physics* **2**, 826 (2006).
- [40] P. Kalpana and K. Jayakumar, in *AIP Conference Proceedings*, Vol. 2220 (AIP Publishing LLC, 2020) p. 100003.
- [41] A. Babanli and B. Ibragimov, *Journal of Magnetism and Magnetic Materials* **495**, 165882 (2020).
- [42] I. Janet Sherly and P. Nithiananthi, *The European Physical Journal Plus* **136**, 1 (2021).
- [43] D. Bartholomew, J. Furdyna, and A. Ramdas, *Physical Review B* **34**, 6943 (1986).
- [44] H. Jimenez-Gonzalez, R. Aggarwal, and P. Becla, *Physical Review B* **45**, 14011 (1992).
- [45] Y. Hwang, H. Kim, S. Cho, Y. Um, H. Park, and G. Jeon, *Journal of Magnetism and Magnetic Materials* **304**, e312 (2006).
- [46] S. Hugonnard-Bruyere, C. Buss, F. Vouilloz, R. Frey, and C. Flytzanis, *Physical Review B* **50**, 2200 (1994).
- [47] C. Buss, R. Pankoke, P. Leisching, J. Cibert, R. Frey, and C. Flytzanis, *Physical review letters* **78**, 4123 (1997).
- [48] K. Nakamura and H. Nakano, *Journal of the Physical Society of Japan* **59**, 1154 (1990).
- [49] M. Kohl and D. Awschalom, *Journal of applied physics* **70**, 6377 (1991).
- [50] C. Buss, R. Frey, C. Flytzanis, and J. Cibert, *Solid state communications* **94**, 543 (1995).

- [51] C. Gourdon, G. Lazard, V. Jeudy, C. Testelin, E. Ivchenko, and G. Karczewski, *Solid state communications* **123**, 299 (2002).
- [52] H. D. Nelson, L. R. Bradshaw, C. J. Barrows, V. A. Vlaskin, and D. R. Gamelin, *ACS nano* **9**, 11177 (2015).
- [53] P. Kalpana and K. Jayakumar, *Physica Scripta* **94**, 105817 (2019).
- [54] S.-K. Chang, A. Nurmikko, J.-W. Wu, L. Kolodziejski, and R. Gunshor, *Physical Review B* **37**, 1191 (1988).
- [55] S. G. Jayam and K. Navaneethakrishnan, *International Journal of Modern Physics B* **16**, 3737 (2002).
- [56] E. Ivchenko, A. Kavokin, V. Kochereshko, G. Posina, I. Uraltsev, D. Yakovlev, R. Bicknell-Tassius, A. Waag, and G. Landwehr, *Physical Review B* **46**, 7713 (1992).
- [57] S. Wu and S. Tomić, *Journal of Applied Physics* **112**, 033715 (2012).
- [58] V. A. Fonoberov and A. A. Balandin, *Journal of Applied Physics* **94**, 7178 (2003).
- [59] K. Sivalertporn, L. Mouchliadis, A. Ivanov, R. Philp, and E. A. Muljarov, *Physical Review B* **85**, 045207 (2012).
- [60] K. Gnanasekar and K. Navaneethakrishnan, *Modern Physics Letters B* **18**, 419 (2004).
- [61] H. Masterson, J. Lunney, and J. Coey, *Journal of applied physics* **81**, 799 (1997).
- [62] T. Koyanagi, K. Matsubara, H. Takaoka, and T. Takagi, *Journal of applied physics* **61**, 3020 (1987).
- [63] A. Shuvaev, G. Astakhov, A. Pimenov, C. Brüne, H. Buhmann, and L. Molenkamp, *Physical Review Letters* **106**, 107404 (2011).
- [64] K. Nakamura and H. Nakano, *Journal of the Physical Society of Japan* **61**, 1390 (1992).
- [65] S. Kumari and S. Chakraborty, *Journal of Sensors and Sensor Systems* **7**, 421 (2018).
- [66] A. Pollmann, R. Hellmann, E. Göbel, D. Yakovlev, W. Ossau, A. Waag, R. Bicknell-Tassius, and G. Landwehr, *Applied physics letters* **61**, 2929 (1992).
- [67] J. Harris and A. Nurmikko, *Physical review letters* **51**, 1472 (1983).
- [68] P. Kalpana and K. Jayakumar, *Physica E: Low-dimensional Systems and Nanostructures* **93**, 252 (2017).
- [69] I. Akimov, T. Godde, K. Kavokin, D. Yakovlev, I. Reshina, I. Sedova, S. Sorokin, S. Ivanov, Y. G. Kusrayev, and M. Bayer, *Physical Review B* **95**, 155303 (2017).